Smart Structures and Systems, Vol. 10, No. 4-5 (2012) 411-426
DOI: http://dx.doi.org/10.12989/sss.2012.10.4_5.411

SHM benchmark for high-rise structures: a reduced-order finite element model and field measurement data

Y.Q. Ni*[1], Y. Xia[1], W. Lin[1,2], W.H. Chen[1,3] and J.M. Ko[1]

[1]*Department of Civil and Structural Engineering, The Hong Kong Polytechnic University, Hung Hom, Kowloon, Hong Kong*
[2]*College of Civil Engineering, Fuzhou University, Fuzhou, China*
[3]*Department of Applied Mechanics and Engineering, Sun Yat-sen University, Guangzhou, China*

(Received December 21, 2011, Revised April 2, 2012, Accepted May 21, 2012)

Abstract. The Canton Tower (formerly named Guangzhou New TV Tower) of 610 m high has been instrumented with a long-term structural health monitoring (SHM) system consisting of over 700 sensors of sixteen types. Under the auspices of the Asian-Pacific Network of Centers for Research in Smart Structures Technology (ANCRiSST), an SHM benchmark problem for high-rise structures has been developed by taking the instrumented Canton Tower as a host structure. This benchmark problem aims to provide an international platform for direct comparison of various SHM-related methodologies and algorithms with the use of real-world monitoring data from a large-scale structure, and to narrow the gap that currently exists between the research and the practice of SHM. This paper first briefs the SHM system deployed on the Canton Tower, and the development of an elaborate three-dimensional (3D) full-scale finite element model (FEM) and the validation of the model using the measured modal data of the structure. In succession comes the formulation of an equivalent reduced-order FEM which is developed specifically for the benchmark study. The reduced-order FEM, which comprises 37 beam elements and a total of 185 degrees-of-freedom (DOFs), has been elaborately tuned to coincide well with the full-scale FEM in terms of both modal frequencies and mode shapes. The field measurement data (including those obtained from 20 accelerometers, one anemometer and one temperature sensor) from the Canton Tower, which are available for the benchmark study, are subsequently presented together with a description of the sensor deployment locations and the sensor specifications.

Keywords: structural health monitoring; benchmark problem; high-rise structure; finite element model; field monitoring data

1. Introduction

Safety and serviceability are two main concerns for in-service civil engineering structures such as bridges and buildings. In-service structures are subjected to progressive deterioration under continuous normal and occasional excessive loadings and adverse environmental conditions (Aktan *et al*. 2001, Rolander *et al*. 2001, DeWolf *et al*. 2002). SHM systems seek to monitor the critical responses of structures and surrounding environment, and detect possible damage which may affect structural safety and serviceability (Catbas and Aktan 2002, Chang *et al*. 2003, Wong 2004, Ko and

*Corresponding author, Professor, E-mail: ceyqni@polyu.edu.hk

Ni 2005, Brownjohn 2007, Fujino *et al*. 2009, Glisic *et al*. 2009, Ou and Li 2009, Wang and Yim 2010, Yun *et al*. 2011). There has been rapid development of SHM technology over the past two decades. A variety of SHM and damage detection methods have been proposed by different investigators (Doebling *et al*. 1998, Carden and Fanning 2004, Sohn *et al*. 2004, Adewuyi *et al*. 2009). However, the feasibility of these methods for real-world applications, especially for applications to large-scale structures, has been rarely examined. A gap still exists between the research and the practice in this field, which impedes broader applications of SHM techniques in civil engineering community. It is significant to establish an SHM benchmark problem in regard to a full-scale structure with the use of field measurement data, aiming to provide an international platform for direct comparison of various algorithms/methods; thus the participants have opportunities to verify their SHM techniques using real-world data from a full-scale structure and recognize the obstructions in real life implementations.

Under the auspices of Asian-Pacific Network of Centers for Research in Smart Structures Technology (ANCRiSST), an SHM benchmark problem for high-rise structures is developed by taking the instrumented Canton Tower of 610 m high as a host structure. This SHM benchmark study aims to provide an open platform to the researchers and practitioners in the field of SHM for examining the applicability and reliability of their methods to a real high-rise structure with the use of field monitoring data. To facilitate the benchmark study, a reduced-order FEM of the Canton Tower has been developed and uploaded together with typical field measurement data acquired from the structure at the benchmark website (http://www.cse.polyu.edu.hk/benchmark/) for the investigation on modal identification, model updating, force identification, SHM-oriented optimal sensor placement, and damage detection. This paper describes the development of the reduced-order FEM, which is tuned in good agreement with an elaborate full-scale 3D model of the Canton Tower in terms of the modal properties (updating the reduced-order FEM to reconcile the predicted modal properties with the field-measured modal properties remains as a task of the benchmark study), and the field measurement data available for this benchmark study.

2. SHM system for Canton Tower

The Canton Tower located in Guangzhou, China, assures a place among the supertall structures worldwide by virtue of its total height of 610 m. As shown in Fig. 1(a), it consists of a 454 m high main tower and a 156 m high antenna mast. The main tower is a tube-in-tube structure consisting of a steel lattice outer structure and a reinforced concrete inner structure. The outer structure has a hyperboloid form, which is generated by the rotation of two ellipses, one at the ground level and the other at an imaginary horizontal plan 454 m above the ground. The tightening caused by the rotation between the two ellipses forms the characterizing "waist-line" of the tower. The cross-section of the outer structure is 50×80 m at the ground, 20.65×27.5 m (minimum) at the waist level (280 m high), and 41×55 m at the top (454 m high). The outer structure is made of 24 inclined concrete-filled-tube steel columns, which are transversely interconnected by steel ring beams and bracings. The inner structure is an ellipse shape as well with a constant cross-section of 14×17 m throughout the height. The centroids of the outer structure and the inner structure are different in the plane. The inner and outer structures are connected at 37 floors. The antenna mast is a steel structure founded on the top of the main tower. The lower part of the antenna mast is a steel lattice structure with an octagon cross-section. The diagonal length of the octagon is 14 m at the bottom

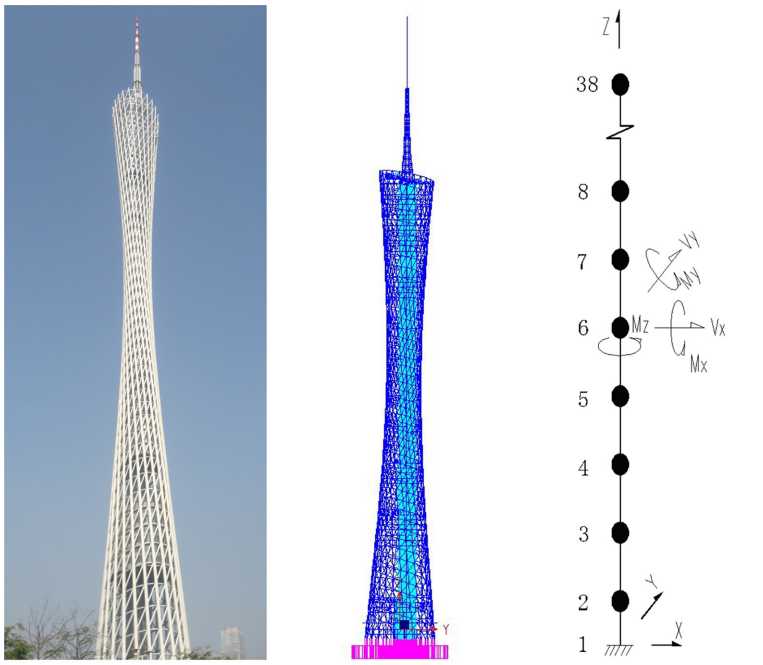

(a) overall view (b) full-scale FEM (c) reduced-order FEM

Fig. 1 The Canton Tower and its FEMs

and decreases as the height rises. The upper part of the antenna mast is a steel box structure. The form of the cross section varies with height, being square, hexagon and square again. The side length of the square cross section on the top of the antenna mast is 0.75 m only. The tower serves for a variety of function – television and radio transmission, sightseeing, catering, and entertainment embracing an orbital Ferris wheel, a ceremony hall, observatory decks, 4D cinemas, revolving restaurants, skywalk, etc. With the completion of construction in May 2009, the Canton Tower was open for operation during the 2010 Asia Games.

To ensure safety and serviceability of this landmark structure during construction and operation, a sophisticated long-term SHM system has been designed and implemented by a joint team from The Hong Kong Polytechnic University and Sun Yat-Sen University for real-time monitoring of the structure at both in-construction and in-service stages (Ni *et al*. 2009, 2011). The integrated in-construction and in-service SHM system consists of over 700 sensors which include a weather station (air temperature, humidity, barometric pressure, rainfall), a total station, a GPS system, a seismograph, accelerometers, anemometers, wind pressure meters, FBG temperature and strain sensors, vibrating wire strain gauges and temperature sensors, electrical resistance temperature sensors, corrosion sensors, digital video cameras, tiltmeters, level sensors, laser zenith meters, and altazimuths. Among them, a total of 200 FBG sensors have been deployed on the main tower and the antenna mast to provide online monitoring of dynamic strain and temperature. A hybrid tethered and wireless data acquisition network in conjunction with 13 data acquisition units (DAUs) during in-construction monitoring and 5 DAUs during in-service monitoring has been adopted in the SHM system. The stress evolution of the structure as construction activity progresses has been studied (Xia *et al*. 2011). Since 2008, the SHM system has successfully monitored seismic responses of the

Canton Tower during nine earthquakes (including the devastating Wenchuan earthquake on 12 May 2008 and Japan earthquake on 11 March 2011), and wind properties around and structural responses of the tower during eight typhoons. These monitoring data are exceedingly useful for detecting anomalies in loading and response and assessing the structural integrity, safety, serviceability, and reliability.

3. Development of reduced-order FEM

3.1 Formulation of full-scale FEM

Based on the design drawings of the Canton Tower, an elaborate full-scale 3D FEM as shown in Fig. 1(b) was first developed as a baseline model. This full-scale model, established with the commercial software ANSYS, consists of 122,476 elements, 84,370 nodes, and 505,164 DOFs in total. In the model, element types PIPE16 and BEAM44 in ANSYS (two-node 3D beam elements with six DOFs at each node) are employed to model the outer structure, antenna mast, and connecting girders between the inner and outer structures. Element type SHELL63 (four-node and three-node shell elements with six DOFs at each node) is used to model the shear walls of the inner structure and floor decks. With this FEM, the modal frequencies and mode shapes of the tower are calculated using the subspace iteration solver routine in ANSYS, as shown in Table 1 and Fig. 2. The validation of this model is then conducted by comparing the predicted modal properties with the identified modal properties through ambient vibration measurement. Table 1 provides a comparison between the predicted and measured modal frequencies. It is observed that the discrepancy is lower than 10% for the two fundamental modes but larger than 10% for the higher modes. Model updating is therefore desired for the model to better represent the real properties of the tower. However, it is very difficult to carry out updating for an FEM involving 505,164 DOFs. To facilitate the model updating and other model-related studies, an equivalent reduced-order FEM is formulated in the next section.

3.2 Formulation of reduced-order FEM

The reduced-order FEM is generated from the full-scale FEM and expected to maintain the main dynamic characteristics of the full-scale model. In formulating the reduced-order FEM, it is assumed that the outer structure and the inner structure are connected by rigid girders and move consistently.

Table 1 Calculated and measured modal frequencies of Canton Tower

Description of mode	Full-scale FEM (Hz)	Ambient vibration test (Hz)	Relative difference
1st short-axis bending	0.110	0.101	8.91%
1st long-axis bending	0.159	0.148	7.43%
2nd short-axis bending	0.400	0.476	15.97%
2nd long-axis bending	0.485	0.534	10.14%
1st torsion	0.461	0.535	13.83%
2nd torsion	1.122	1.271	11.72%

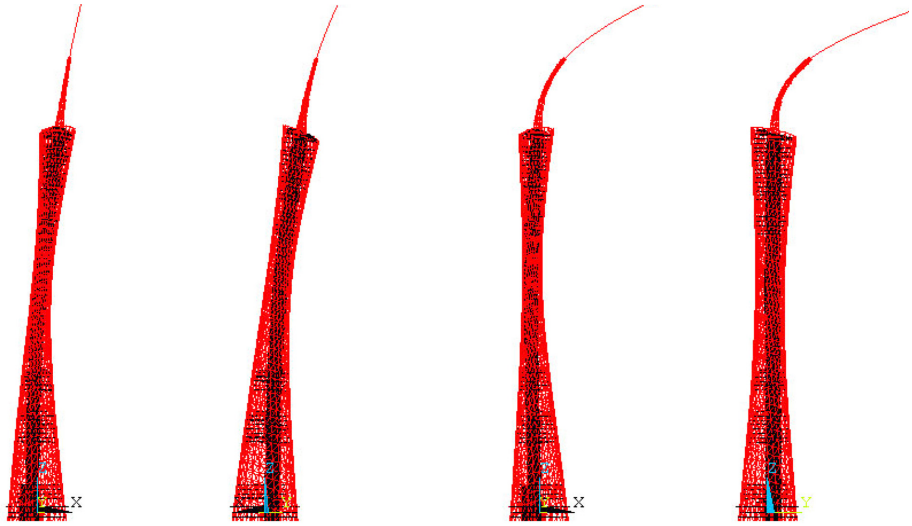

(a) 1st bending mode of main tower (b) 1st bending mode of antenna mast

(c) 2nd bending mode of main tower (d) 1st and 2nd torsional modes

Fig. 2 Mode shapes obtained by full-scale FEM

By doing so, the whole structure can be approximated as a 3D cantilever beam. To achieve this, the entire structure is divided into 37 segments vertically (the number and length of the segments are determined according to the layout of sensors and locations of floors and connecting girders), each being modeled as a 3D linear elastic beam element. Thus the whole structure is characterized by 37 beam elements as shown in Fig. 1(c), with 27 elements for the main tower and 10 elements for the antenna mast. The nodes are numbered from 1 at the fixed base to 38 at the free top end. The node positions (vertical coordinates) are selected by also considering consistent lengths for different elements (segments). Table 2 provides the vertical coordinates of the nodes. The vibration measurement results show that the vertical displacement is much less than the two horizontal displacements for

Table 2 Nodal coordinates (z) in reduced-order model

Node No.	z (m)	Node No.	z (m)	Node No.	z (m)
1	-10.00	14	204.25	27	438.25
2	0.00	15	225.20	28	443.60
3	12.00	16	272.00	29	480.00
4	22.25	17	308.25	30	497.60
5	27.60	18	329.20	31	505.20
6	58.65	19	344.65	32	520.70
7	84.65	20	355.05	33	531.20
8	95.05	21	375.85	34	545.20
9	105.45	22	381.20	35	565.20
10	116.20	23	396.65	36	580.70
11	147.05	24	407.05	37	598.00
12	157.45	25	417.45	38	610.00
13	168.00	26	427.85	-	-

the Canton Tower, and therefore the DOF of vertical translation is disregarded for each node in the reduced-order model. As a result, each node has two horizontally translational DOFs and three rotational DOFs, and the reduced-order model has a total of 185 unconstrained DOFs.

In the reduced-order model, the axis of the beam elements is assigned to align with the centroidal axis of the antenna mast, and the horizontal coordinates of the 38 nominal section centers are also the same (the floor centroid of the real structure varies slightly). The element mass matrices are considered to be lumped mass matrices. Each mass matrix is generated by the following steps:

i) The nodal masses in the full-scale FEM are lumped to the nearest nominal section centers in the reduced-order FEM in consideration of equivalence for both translational and rotational inertias;

ii) The entries in the element mass matrix corresponding to translational DOFs are obtained by summing up all masses lumped at the nominal section center;

iii) The entries in the element mass matrix corresponding to rotational DOFs are calculated by the following equations

$$m_{mx} = \sum_{i=1}^{s} m_i l_{xi}^2 \quad m_{my} = \sum_{i=1}^{s} m_i l_{yi}^2 \quad m_{mz} = \sum_{i=1}^{s} m_i l_{zi}^2 \tag{1a, b, c}$$

where m_{mx}, m_{my} and m_{mz} are the rotational inertias of the element; m_i is the mass lumped at node i of the full-scale model; and l_x, l_y and l_z are the projective distances between node i and the nearest nominal section center.

The element stiffness matrix of the reduced-order FEM is generated from the full-scale FEM by the following steps:

i) For each beam element, the corresponding segment between two horizontal sections is selected from the full-scale model. All the nodes on the two sections are constrained;

ii) To calculate the stiffness coefficients of the j^{th} column of $\boldsymbol{K}^e$, a unit displacement is imposed on the j^{th} DOF of the segment while all other displacements are constrained. Here j=1, 2, …, 10. j=1 to 5 refer to the lateral translational displacements in x and y directions, and rotations about x, y and z axes at the lower node, respectively. Similarly j=6 to 10 refer to the displacements and rotations at the upper node. Fig. 3(a) illustrates the case of j=1, where all nodes at the upper section are

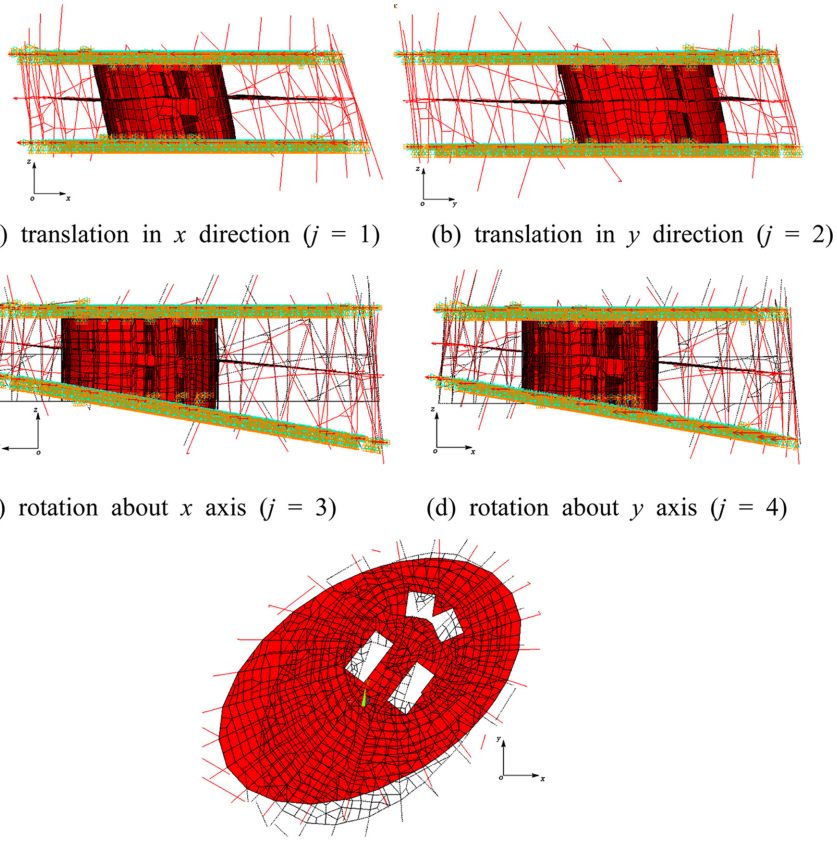

(a) translation in x direction (j = 1) (b) translation in y direction (j = 2)

(c) rotation about x axis (j = 3) (d) rotation about y axis (j = 4)

(e) rotation about z axis (j = 5)

Fig. 3 Unit displacement imposed in different directions

constrained and all nodes at the lower section are imposed by a unit displacement in x direction simultaneously. The cases of j=2 to 5 are shown in Figs. 3(b) to 3(e), respectively. It is noted that when j=3, 4, and 5, the corresponding translational displacements should be first calculated and applied to the nodes;

iii) The resultant generalized force at the i^{th} DOF of the segment due to the unit displacement at the j^{th} DOF is calculated and denoted as $\boldsymbol{K}_{ij}$ of the beam element. Here i=1, 2, …, 10. Correspondingly, i=1 to 5 refer to the shear forces in x and y directions and moments (torque) about x, y and z axes at the lower node, respectively. i=6 to 10 refer to the force components at the upper node.

After repeating the above steps to obtain mass and stiffness matrices for all elements, the element mass and stiffness matrices are assembled to obtain the global mass and stiffness matrices of the reduced-order FEM.

3.3 Refinement of reduced-order FEM

The modal properties of the reduced-order model inevitably differ from those of the full-scale model due to simplification. As evidenced in Table 3, the frequency discrepancy between the full-scale and reduced-order models is quite large for some modes. In the following, the reduced-order

Table 3 Comparison of modal frequencies between full-scale FEM and reduced-order FEM

Description of mode	Full-scale FEM (Hz)	Reduced-order FEM (Hz)	Relative difference
1st short-axis bending	0.110	0.123	11.82%
1st long-axis bending	0.159	0.163	2.52%
2nd short-axis bending	0.400	0.423	5.75%
2nd long-axis bending	0.485	0.439	9.48%
1st torsion	0.461	0.523	13.45%
2nd torsion	1.122	1.318	17.47%

model is tuned using a sensitivity-based model updating method to make the modal properties (modal frequencies and mode shapes) of the reduced-order model well match with the counterparts of the full-scale model (updating the reduced-order model to reconcile the predicted modal properties with the field-measured modal properties remains as a task of the benchmark study).

In the sensitivity-based model updating method (Görl and Link 2003, Lu and Law 2007), the basic equation has the form

$$\delta \boldsymbol{J} = \boldsymbol{S} \cdot \delta \boldsymbol{P} \tag{2}$$

where $\delta \boldsymbol{P}$ is the perturbation in the model parameters, $\delta \boldsymbol{J}$ is the error vector in the measured output, and $\boldsymbol{S}$ is the sensitivity matrix. In the present study, the residual vector to be minimized is taken as

$$J = \boldsymbol{R}^T \boldsymbol{W} \boldsymbol{R} \tag{3}$$

where $\boldsymbol{W}$ is a diagonal weighting matrix; $\boldsymbol{R} = \{\boldsymbol{R}^Q \quad \boldsymbol{R}^S\}^T$; $\boldsymbol{R}^Q$ and $\boldsymbol{R}^S$ represent the frequency differences and the mode shape similarities between the full-scale and reduced-order models, which are respectively expressed as

$$\boldsymbol{R}^Q(i) = \frac{\left| f_i^F - f_i^R \right|}{f_i^F} \tag{4}$$

$$\boldsymbol{R}^S(i) = 1 - MAC(i) \tag{5}$$

$$MAC(i) = \frac{\{\varphi_i^F\}^T \{\varphi_i^R\}}{(\{\varphi_i^F\}^T \{\varphi_i^F\})(\{\varphi_i^R\}^T \{\varphi_i^R\})} \tag{6}$$

where f_i denotes the i^{th} modal frequency; φ_i is the i^{th} mode shape; the superscripts 'F' and 'R' represent the items associated with the full-scale and reduced-order models, respectively; and the superscript 'T' denotes vector (matrix) transpose.

As the outer structure and the inner structure of the Canton Tower move consistently, the normalized bending mode shape values of the full-scale model are obtained by averaging the modal displacement components of the nodes in the inner structure. For the torsional modes, the normalized mode shape values of the full-scale model are calculated by averaging the rotation angles of all nodes in the inner structure with respect to the corresponding nominal section center. The modal frequencies and mode shapes of the first fifteen modes are included in the updating. The relative weights of frequencies and mode shapes affect the model updating results significantly and

should be chosen carefully. The weight coefficients are selected according to the accuracy of the measurement and the importance of the quantities. Since the mode shape measurements are usually less accurate than the natural frequencies, the weights for the mode shapes are smaller than those for the frequencies (Hao and Xia 2002). In addition, the higher modes may be measured less accurate than the lower modes. As a result, here the weight coefficients are set to 10 for all frequencies ($\boldsymbol{R}^Q$), 1.0 for the first four bending mode shapes and the first two torsional mode shapes ($\boldsymbol{R}^S$), 0.5 for the next four bending mode shapes, and 0.3 for other five higher-order mode shapes. As the full-scale model contains many nodes at each floor and their mode shape components may differ with each other, the mode shape values are averaged and treated as the mode shape component of the corresponding node in the reduced-order model.

As mentioned before, the Canton Tower is asymmetric and the geometric centroid of each floor varies. Each element in the reduced-order model was assigned to align with the centriodal axis of the antenna mast. Consequently, the element stiffness matrix in the reduced-order model differs from that of an Euler-Bernoulli beam. This causes much error in the reduced-order model. In this regard, the mass matrices are assumed correct and only the element stiffness matrices are adjusted in the updating process. In this study, two coefficients α_E and α_G are introduced as the updating parameters for each element stiffness matrix, resulting in a total of 74 unknowns to be updated. α_E represents the modulus variation coefficient that is associated with all entries in the element stiffness matrix, while α_G is associated with bending and rotational DOFs only. As a result, a typical updated element stiffness matrix can be expressed as

$$\mathbf{K}_U^e = \begin{bmatrix} \alpha_E\mathbf{K}_{11}^e & \alpha_E\mathbf{K}_{12}^e & \alpha_E\alpha_G\mathbf{K}_{13}^e & \alpha_E\alpha_G\mathbf{K}_{14}^e & \alpha_E\alpha_G\mathbf{K}_{15}^e & \alpha_E\mathbf{K}_{16}^e & \alpha_E\mathbf{K}_{17}^e & \alpha_E\alpha_G\mathbf{K}_{18}^e & \alpha_E\alpha_G\mathbf{K}_{19}^e & \alpha_E\alpha_G\mathbf{K}_{110}^e \\ & \alpha_E\mathbf{K}_{22}^e & \alpha_E\alpha_G\mathbf{K}_{23}^e & \alpha_E\alpha_G\mathbf{K}_{24}^e & \alpha_E\alpha_G\mathbf{K}_{25}^e & \alpha_E\mathbf{K}_{26}^e & \alpha_E\mathbf{K}_{27}^e & \alpha_E\alpha_G\mathbf{K}_{28}^e & \alpha_E\alpha_G\mathbf{K}_{29}^e & \alpha_E\alpha_G\mathbf{K}_{210}^e \\ & & \alpha_E\alpha_G\mathbf{K}_{33}^e & \alpha_E\alpha_G\mathbf{K}_{34}^e & \alpha_E\alpha_G\mathbf{K}_{35}^e & \alpha_E\alpha_G\mathbf{K}_{36}^e & \alpha_E\alpha_G\mathbf{K}_{37}^e & \alpha_E\alpha_G\mathbf{K}_{38}^e & \alpha_E\alpha_G\mathbf{K}_{39}^e & \alpha_E\alpha_G\mathbf{K}_{310}^e \\ & & & \alpha_E\alpha_G\mathbf{K}_{44}^e & \alpha_E\alpha_G\mathbf{K}_{45}^e & \alpha_E\alpha_G\mathbf{K}_{46}^e & \alpha_E\alpha_G\mathbf{K}_{47}^e & \alpha_E\alpha_G\mathbf{K}_{48}^e & \alpha_E\alpha_G\mathbf{K}_{49}^e & \alpha_E\alpha_G\mathbf{K}_{410}^e \\ & & & & \alpha_E\alpha_G\mathbf{K}_{55}^e & \alpha_E\alpha_G\mathbf{K}_{56}^e & \alpha_E\alpha_G\mathbf{K}_{57}^e & \alpha_E\alpha_G\mathbf{K}_{58}^e & \alpha_E\alpha_G\mathbf{K}_{59}^e & \alpha_E\alpha_G\mathbf{K}_{510}^e \\ & & & & & \alpha_E\mathbf{K}_{66}^e & \alpha_E\mathbf{K}_{67}^e & \alpha_E\alpha_G\mathbf{K}_{68}^e & \alpha_E\alpha_G\mathbf{K}_{69}^e & \alpha_E\alpha_G\mathbf{K}_{610}^e \\ & & \text{Symmetric} & & & & \alpha_E\mathbf{K}_{77}^e & \alpha_E\alpha_G\mathbf{K}_{78}^e & \alpha_E\alpha_G\mathbf{K}_{79}^e & \alpha_E\alpha_G\mathbf{K}_{710}^e \\ & & & & & & & \alpha_E\alpha_G\mathbf{K}_{88}^e & \alpha_E\alpha_G\mathbf{K}_{89}^e & \alpha_E\alpha_G\mathbf{K}_{810}^e \\ & & & & & & & & \alpha_E\alpha_G\mathbf{K}_{99}^e & \alpha_E\alpha_G\mathbf{K}_{910}^e \\ & & & & & & & & & \alpha_E\alpha_G\mathbf{K}_{1010}^e \end{bmatrix} \quad (7)$$

where $\boldsymbol{K}_U^e$ and $\boldsymbol{K}^e$ are the updated and initial element stiffness matrices, respectively.

The objective function defined in Eq. (3) with the constraints that $0.1 \le \alpha_E, \alpha_G \le 10$ is minimized using the sensitivity-based updating algorithm. During the model updating, the modal data of the full-scale model is the target while the reduced-order model is updated. The sensitivity matrix and the error vector in Eq. (2) are calculated from the reduced-order model, from which increments of the updating parameters are also obtained. The reduced-order model is then updated and the corresponding modal data and its sensitivity are computed for the next iteration. Convergence is achieved when $\|\boldsymbol{J}\|$ reaches a value lower than the pre-defined tolerance.

3.4 Modal properties of reduced-order FEM after refinement

The modal properties obtained from the full-scale model and from the reduced-order model after refinement are listed in Table 4. A comparison of mode shapes for the first fifteen modes is provided in Fig. 4. It is seen that the modal properties (both modal frequencies and mode shapes)

Table 4 Comparison of modal properties between full-scale FEM and refined reduced-order FEM

Mode No.	Full-scale model	Modal frequency (Hz)		MAC
		Reduced-order model	Relative difference	
1	0.110	0.110	0.00%	99.98%
2	0.159	0.159	0.00%	99.97%
3	0.347	0.347	0.00%	99.53%
4	0.368	0.368	0.00%	99.52%
5	0.400	0.399	0.25%	99.55%
6	0.461	0.460	0.22%	99.86%
7	0.485	0.485	0.00%	99.39%
8	0.738	0.738	0.00%	99.29%
9	0.902	0.902	0.00%	99.36%
10	0.997	0.997	0.00%	99.43%
11	1.038	1.038	0.00%	98.99%
12	1.122	1.122	0.00%	99.41%
13	1.244	1.244	0.00%	98.31%
14	1.503	1.503	0.00%	96.76%
15	1.726	1.726	0.00%	97.50%

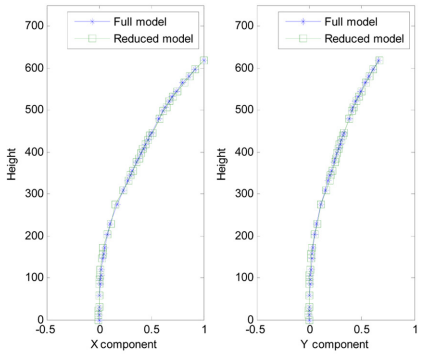

(a) 1st mode (1st short-axis bending)

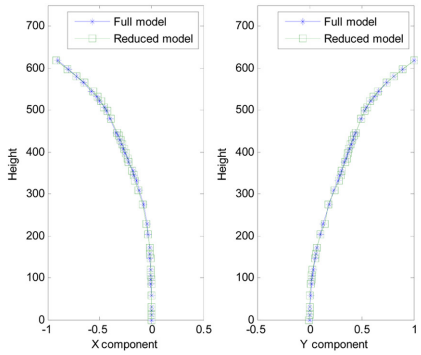

(b) 2nd mode (1st long-axis bending)

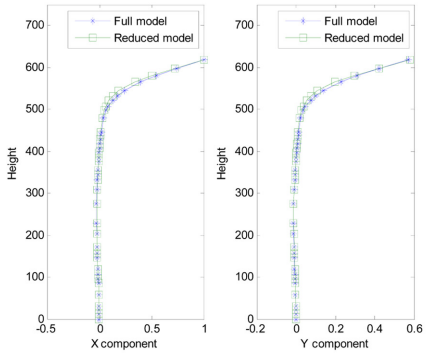

(c) 3rd mode (1st short-axis bending of mast)

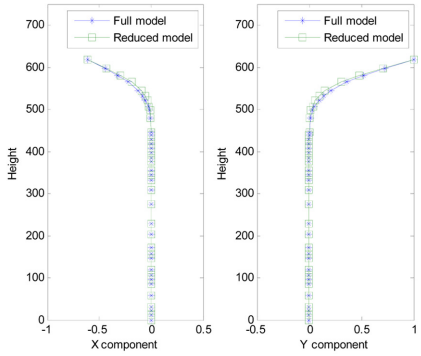

(d) 4th mode (1st long-axis bending of mast)

Fig. 4 Comparison of mode shapes between full-scale FEM and refined reduced-order FEM

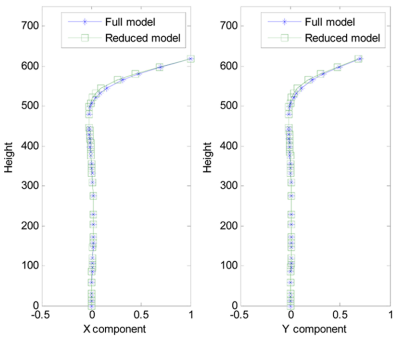

(e) 5th mode (2nd short-axis bending)

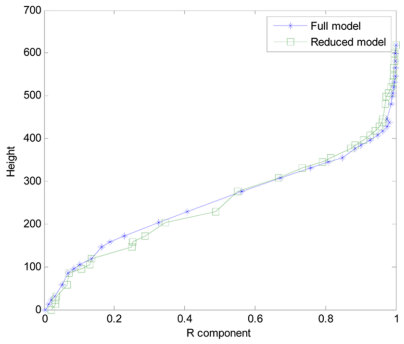

(f) 6th mode (1st torsion)

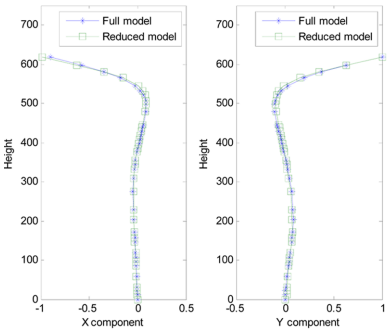

(g) 7th mode (2nd long-axis bending)

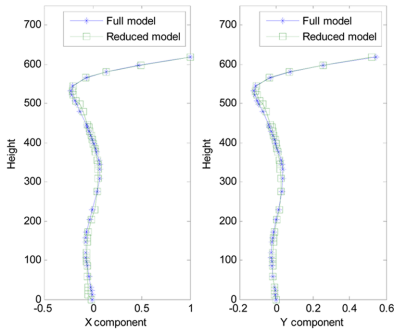

(h) 8th mode (3rd short-axis bending)

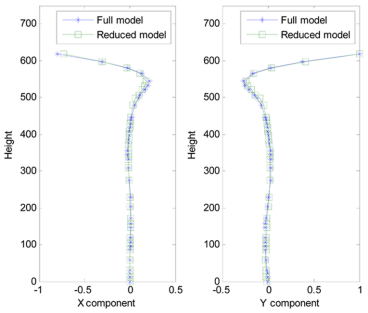

(i) 9th mode (3rd long-axis bending)

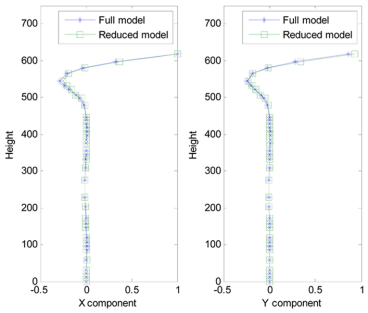

(j) 10th mode (2nd short-axis bending of mast)

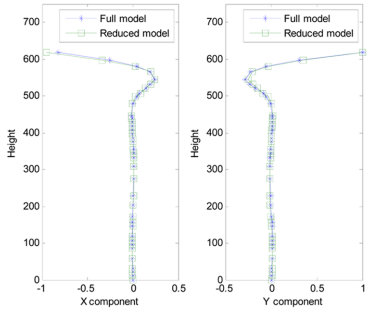

(k) 11th mode (2nd long-axis bending of mast)

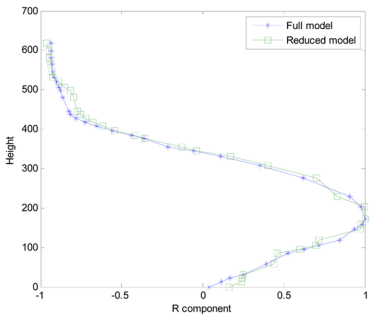

(l) 12th mode (2nd torsion)

Fig. 4 Continued

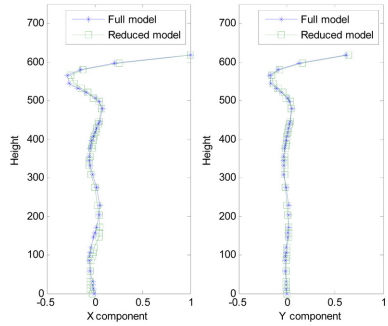

(m) 13th mode (coupled bending and torsion)

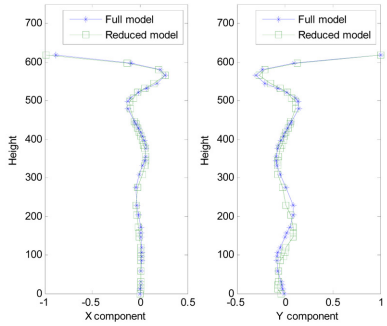

(n) 14th mode (coupled bending and torsion)

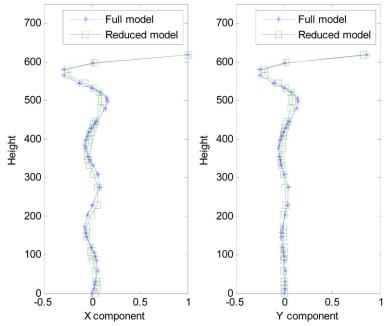

(o) 15th mode (coupled bending and torsion)

Fig. 4 Continued

obtained from the two models are in excellent agreement for the first fifteen modes.

4. Field measurement data

The field monitoring data from the accelerometers, anemometer, and temperature sensor deployed on the Canton Tower has been uploaded to the SHM benchmark website. As part of the long-term SHM system, more than 20 uni-axial accelerometers (Tokyo Sokushin AS-2000C) have been permanently installed for structural dynamic response measurement. The frequency range is DC-50 Hz (3 dB), amplitude range ±2 g, and the sensitivity 1.25 V/g for the accelerometers. One anemometer (RM Young, 05103L) is positioned on the top of the main tower to measure the wind direction and wind speed. The measurement range is 0~100 m/s and output signal is electric current type so that the signal can be transmitted to the data acquisition unit about 100 m away. One thermocouple (PT100) is installed near the anemometer to measure the air temperature.

Nine sections at different heights of the structure have been selected to place the accelerometers. 20 accelerometers are deployed at eight levels of the main tower as shown in Fig. 5 after considering the availability of space and access to the data acquisition units. For example, the first section is at the height of 30.63 m, 3.03 m above the floor at 27.6 m. In the 4th and 8th levels, each section has four uni-axial accelerometers: two for the measurement of horizontal vibrations along the long-axis of the inner structure and the other two along the short-axis of the inner structure. At other six levels, each section is equipped with two uni-axial accelerometers: one along the long-axis of the inner structure and the other along the short-axis of the inner structure. Fig. 6 illustrates the measurement positions and directions at different sections.

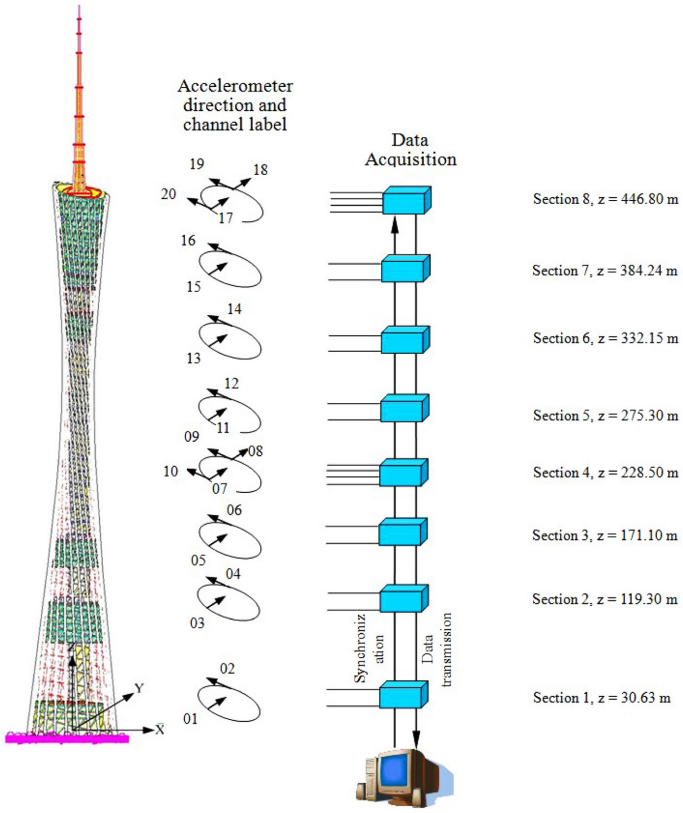

Fig. 5 Deployment of accelerometers and data acquisition system on Canton Tower

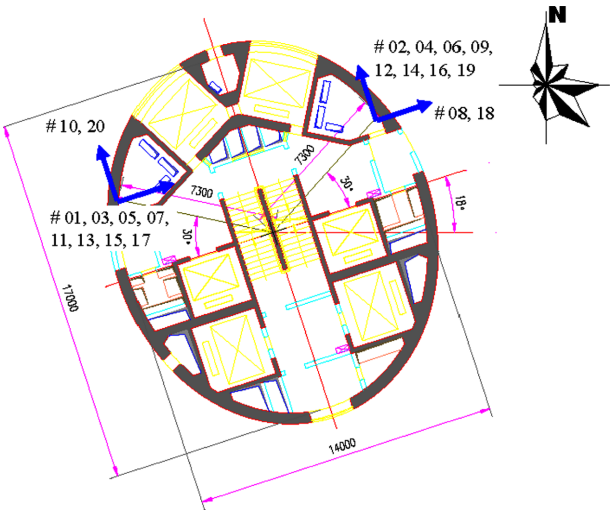

Fig. 6 Measurement positions and directions of accelerometers at different sections

Accelerometers have also been installed on the antenna mast. However, the data from the accelerometers positioned at the antenna mast has not been included in the data set that has been

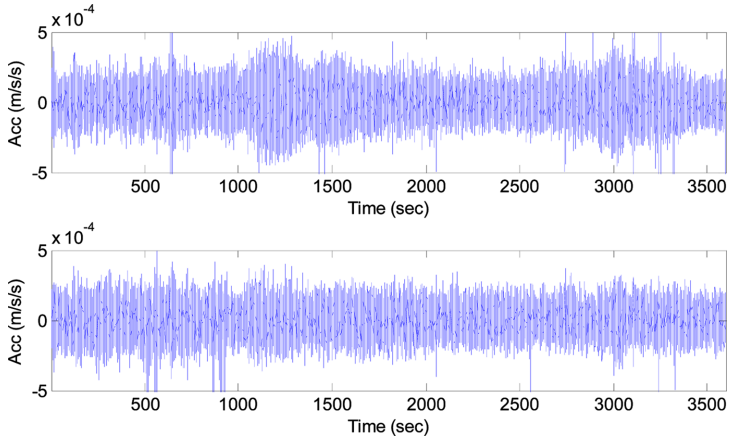

Fig. 7 Measurement data of acceleration (top: Channel No. 18; bottom: Channel No. 19)

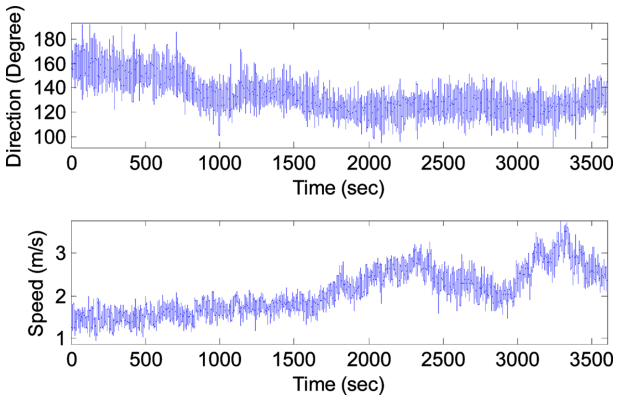

Fig. 8 Measurement data of wind (top: wind direction; bottom: wind speed)

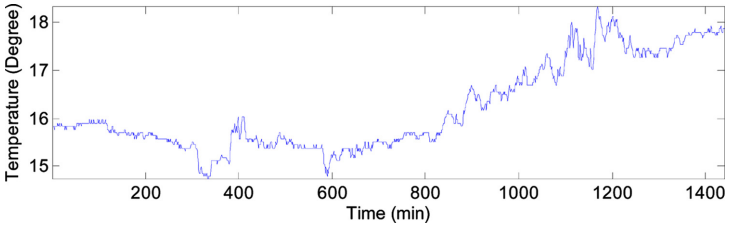

Fig. 9 Measurement data of air temperature

uploaded at the benchmark website. The field measurement data from other accelerometers deployed at the eight levels of the main tower, lasting for 24 hours in ambient vibration condition, together with the corresponding data from the anemometer and the temperature sensor, are now available at the website (http://www.cse.polyu.edu.hk/benchmark/index.htm). Figs. 7 to 9 show the time histories of the measured acceleration, wind direction and wind speed, and temperature. Because the structural dynamic responses (acceleration and dynamic strain) of the Canton Tower under a number of typhoon and earthquake events have been acquired, the data obtained during the extreme events

will further be shared with collaborators for advanced SHM investigations.

5. Conclusions

Taking the instrumented Canton Tower of 610 m high as a host structure, an SHM benchmark problem for high-rise structures has been developed and shared with interested investigators worldwide. This paper detailed the formulation and refinement of a reduced-order FEM of the host structure and the field measurement data (including acceleration, wind speed and direction, and temperature) acquired from the host structure. In addition to the field measurement data, the reduced-order FEM has been uploaded to the benchmark website with individual element mass and stiffness matrices to facilitate the SHM-related study. With the provided reduced-order model and field measurement data, participants can pursue the investigation on modal identification, model updating, force identification, SHM-oriented optimal sensor placement, and damage detection. It is anticipated that the participants of this benchmark study, when they publish research results on the benchmark study, can provide detailed information about the following issues: (i) methodology and underlying assumptions; (ii) evaluation and verification criteria (including convergence criteria if appropriate); (iii) type of information used (time-domain data or modal data; how long time-history data or how many modes used); (iv) quantification of the updating and identification results; and (v) comparison with the available methods/results. The above information shall be helpful for better understanding and reasonably evaluating the efficiency of different algorithms/methods.

Acknowledgements

The work described in this paper was supported in part by a grant from the Research Grants Council of the Hong Kong Special Administrative Region, China (Project No. PolyU 5263/08E) and partially by a grant from The Hong Kong Polytechnic University through the Development of Niche Areas Programme (Project No. 1-BB68).

References

Adewuyi, A.P., Wu, Z.S. and Serker, N.H.M.K. (2009), "Assessment of vibration-based damage identification methods using displacement and distributed strain measurements", *Struct. Health Monit*., **8**, 443-461.

Aktan, A.E., Chase, S., Inman, D. and Pines, D.D. (2001), "Monitoring and managing the health of infrastructure systems", in: Health Monitoring and Management of Civil Infrastructure Systems, (Eds. Chase, S.B. and Aktan, A.E.), *Proceedings of the SPIE Vol. 4337*, SPIE, Bellingham, Washington, USA (CD-ROM).

Brownjohn, J.M.W. (2007), "Structural health monitoring of civil infrastructure", *Philos. T. R. Soc. A*., **365**(1851), 589-622.

Carden, E.P. and Fanning, P. (2004), "Vibration based condition monitoring: a review", *Struct. Health Monit*., **3**(4), 355-377.

Catbas, F.N. and Aktan, A.E. (2002), "Condition and damage assessment: issues and some promising indices", *J. Struct. Eng.- ASCE*, **128**(8), 1026-1036.

Chang, P.C., Flatau, A. and Liu, S.C. (2003), "Health monitoring of civil infrastructure", *Struct. Health Monit*., **2**, 257-267.

DeWolf, J.T., Lauzon, R.G. and Culmo, M.P. (2002), "Monitoring bridge performance", *Struct. Health Monit*., **1**(2), 129-138.

Doebling, S.W., Farrar, C.R. and Prime, M.B. (1998), "A summary review of vibration-based damage identification

methods", *Shock Vib*., **30**, 91-105.
Fujino, Y., Siringoringo, D.M. and Abe, M. (2009), "The needs for advanced sensor technologies in risk assessment of civil infrastructures", *Smart Struct. Syst*., **5**(2), 173-191.
Glisic, B., Inaudi, D. and Casanova, N. (2009), "SHM process lessons learned in 250 SHM projects", in: *Proceedings of the 4th International Conference on Structural Health Monitoring and Intelligent Infrastructure*, Zurich, Switzerland (CD-ROM).
Görl, E. and Link, M. (2003), "Damage identification using changes of eigenfrequencies and mode shapes", *Mech. Syst. Signal Pr*., **17**(1), 103-110.
Hao, H. and Xia, Y. (2002), "Vibration-based damage detection of structures by genetic algorithm", *J. Comput. Civil Eng*., **16**(3), 222-229.
Ko, J.M. and Ni, Y.Q. (2005), "Technology developments in structural health monitoring of large-scale bridges", *Eng. Struct*., **27**(12), 1715-1725.
Lu, Z.R. and Law, S.S. (2007), "Features of dynamic response sensitivity and its application in damage detection", *J. Sound Vib*., **303**(1-2), 305-329.
Ni, Y.Q., Wong, K.Y. and Xia, Y. (2011), "Health checks through landmark bridges to sky-high structures", *Adv. Struct. Eng*., **14**(1), 103-119.
Ni, Y.Q., Xia, Y., Liao, W.Y. and Ko, J.M. (2009), "Technology innovation in developing the structural health monitoring system for Guangzhou New TV Tower", *Struct. Control Health Monit*., **16**(1), 73-98.
Ou, J. and Li, H. (2009), *Structural health monitoring research in China: trends and applications*, in: Structural Health Monitoring of Civil Infrastructure Systems, (Eds., Karbhari, V.M. and Ansari, F.), Woodhead Publishing, Cambridge, UK, 463-516.
Rolander, D.D., Phares, B.M., Graybeal, B.A., Moore, M.E. and Washer, G.A. (2001), "Highway bridge inspection: state-of-the-practice survey", *Transport. Res. Record*, **1749**, 73-81.
Sohn, H., Farrar, C.R., Hemez, F.M., Shunk, D.D., Stinemates, D.W., Nadler, B.R. and Czarnecki, J.J. (2004), *A review of structural health monitoring literature: 1996-2001*, Los Alamos National Laboratory, Report LA-13976-MS, Los Alamos, USA.
Wang, M.L. and Yim, J. (2010), "Sensor enriched infrastructure system", *Smart Struct. Syst*., **6**(3), 309-333.
Wong, K.Y. (2004), "Instrumentation and health monitoring of cable-supported bridges", *Struct. Control Health Monit*., **11**(2), 91-124.
Xia, Y., Ni, Y.Q., Zhang, P, Liao, W.Y. and Ko, J.M. (2011), "Stress development of a super-tall structure during construction: field monitoring and numerical analysis", *Comput. Aided Civil Infrastruct. Eng*., **26**(7), 542-559.
Yun, C.B., Lee, J.J. and Koo, K.Y. (2011), "Smart structure technologies for civil infrastructures in Korea: recent research and applications", *Struct. Infrastruct. Eng*., **7**(9), 673-688.